Supporting Information for

Optomagnetic Detection of MicroRNA Based on Duplex-Specific Nuclease Assisted Target Recycling and Multilayer Core-Satellite Magnetic Superstructures

Bo Tian,[†] Jing Ma,[‡] Zhen Qiu,[†] Teresa Zardán Gómez de la Torre,[†] Marco Donolato,[§] Mikkel Fougt Hansen,[#] Peter Svedlindh,[†] and Mattias Strömberg*,[†]

[†] Department of Engineering Sciences, Uppsala University, The Ångström Laboratory, Box 534, SE-751 21 Uppsala, Sweden

[‡] Department of Immunology, Genetics and Pathology, Uppsala University, The Rudbeck Laboratory, SE-751 85 Uppsala, Sweden

[§] BluSense Diagnostics, Fruebjergvej 3, DK-2100 Copenhagen, Denmark

[#] Department of Micro- and Nanotechnology, Technical University of Denmark, DTU Nanotech, Building 345B, DK-2800 Kongens Lyngby, Denmark

Table of Contents

S-2. **S1.** Optomagnetic system description and optomagnetic measurement principle.

S-3. **Figure S1.** Schematic illustration of the optomagnetic setup.

S-6. **Figure S2.** Comparison of susceptibility data and optomagnetic data.

S-7. **Table S1.** Sequences of oligonucleotides used in this study.

S-8. **Figure S3.** Scanning electron micrographs of core-satellite superstructures.

S-9. **S2.** Determination of the binding ratios between MPs and MNPs.

S-9. **Figure S4.** Standard curves for MNPs suspended in reaction buffer.

S-10. **Table S2.** Concentrations of MNPs before and after DSN assisted target recycling.

S-11. **Figure S5.** Specificity study of the MP-NP_{80}-based let-7b detection system.

S-12. **Figure S6.** Stability study of the optomagnetic detection system in fetal bovine serum.

S-13. **Figure S7.** Qualitative duplex detection in 20% fetal bovine serum.

S-14. **Figure S8.** Detection of endogenous let-7b from MCF-7 and A549.

S-15. **Figure S9.** Quantitative singleplex detection based on filter-treated MP-NP_{80}.

S1. Optomagnetic system description and optomagnetic measurement principle.

As illustrated in **Figure S1**, the set-up employed for optomagnetic effect measurement was based on an unfocused 405 nm laser source (Sony optical unit, Sony, JP) and a photodetector (PDA36A, Thorlabs Inc., U.S.A.). Powered by a software controlled current source, the laser source provided a linearly polarized light beam (diameter of 2 mm), and the polarization direction was oriented along the axis of the applied magnetic field. A disposable UV-transparent cuvette (REF 67.758.001, SARSTEDT, Nümbrecht, Germany) was positioned in the beam path, centred between a pair of electromagnets (1433428C, Murata Power Solutions Inc., U.S.A.). The optical path through the liquid in the cuvette was 10 mm. The distance between the electromagnets was 20 mm, and the distance between laser source and detector was 115 mm. The LabVIEW controlled electromagnets were powered by an AC source. The AC magnetic field was applied perpendicular to the laser beam, and the maximum AC magnetic field amplitude was limited to approximately 2.6 mT in the current set-up. The self-inductance of the electromagnets was corrected for to ensure constant field amplitude and phase at all frequencies. The laser, electromagnets, cuvette, and detector were covered during measurements to avoid interference from external light sources. The detector signal was converted from analogue to digital by a data acquisition unit (DAQ unit, NI USB-6341, National Instruments, U.S.A.), followed by further processing in the computer by a FFT enabled lock-in function.

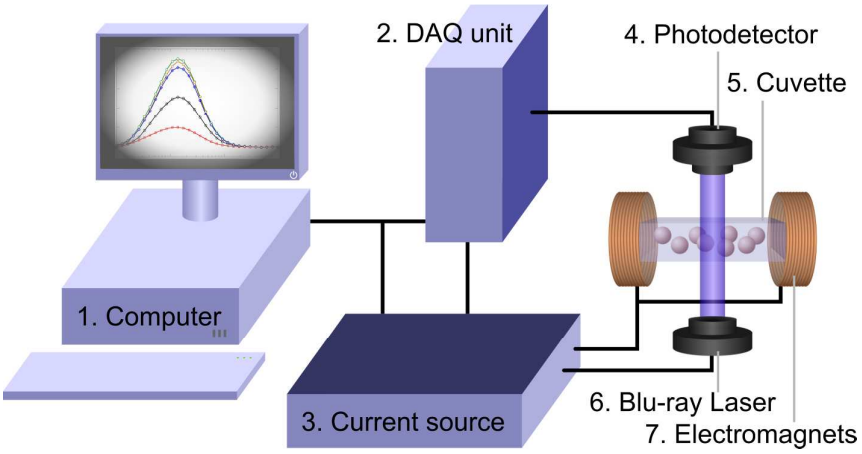

Figure S1. Schematic illustration of the optomagnetic set-up. The liquid sample, contained in an optically transparent cuvette (5), is placed between two identical electromagnets (7). A 405 nm laser source (6) generates a laser beam aimed at the bottom of the cuvette. The transmitted light detected by a photo detector (4) is recorded vs time using a DAQ unit (2). The laser and electromagnets are powered by a current source (3). A computer (1) controls the entire set-up and performs the software based lock-in detection.

The optomagnetic measurement principle is based on the rotational dynamics of magnetic nanoparticles (MNPs). The MNPs employed in this study have a remanent magnetic moment, which implies that the dominating relaxation mechanism upon a reversal of the magnetic field direction is a physical rotation of the particle, known as Brownian relaxation. The characteristic frequency for Brownian relaxation dynamics is given by

$$f_B = \frac{k_B T}{6\pi\eta V_h}, \tag{1}$$

where $k_B T$ is the thermal energy, η is the dynamic viscosity and V_h is the hydrodynamic volume of the relaxing entity (*e.g.*, a single MNP). The dynamic magnetic behavior can be described in term of the magnetic susceptibility χ with real (in-phase) and imaginary (out-of-phase) parts χ' and χ'', respectively. In case of a sinusoidal magnetic field $h_0 \sin(\omega t)$, the time dependent linear magnetic response can be expressed as

$$\chi(t) = M(t)/h_0 = \chi_0 \sin(\omega t - \theta) = \chi' \sin(\omega t) + \chi'' \cos(\omega t), \tag{2}$$

where $\chi' = \chi_0 \cos(\theta)$ and $\chi'' = \chi_0 \sin(\theta)$. At low frequencies the MNPs are able to rotate and follow the magnetic field, and the response is in-phase with the applied field. Therefore χ' is maximal. The rotation of the MNPs starts to lag behind the applied field at higher frequencies, which leads to a decrease in the in-phase component χ' and a corresponding increase in the out-of-phase component χ''. The out-of-phase component χ'' attains its maximum value at the Brownian relaxation frequency f_B.

A simple approach to account for a distribution of MNP sizes was introduced by Cole and Cole[1] according to the following expression for the complex magnetic susceptibility

$$\chi(\omega) - \chi_\infty = \frac{\chi_0 - \chi_\infty}{1 + (i\omega\tau_B)^{1-\alpha}}, \tag{3}$$

where α is the Cole-Cole parameter (ranging from 0 to 1, a measure of the nanoparticle size distribution width), $\tau_B = (f_B)^{-1}$ is the Brownian relaxation time, $\omega = 2\pi f$ is the angular frequency of the applied field and χ_0 and χ_∞ are the zero and high frequency limits of χ.

The dynamics is determined by the rotational behavior of the individual MNPs, which follows the Brownian relaxation dynamics. The modulation of the transmitted light is found in the complex second harmonic voltage output from the photodetector

$$V_2 = V_2' + \mathrm{i}V_2'', \tag{4}$$

where V_2' and V_2'' are the in-phase and out-of-phase signals, respectively. The modulation is measured using a lock-in amplifier with the AC magnetic field excitation as reference. From the perspective of transmitted light, the MNP ensemble will scatter light equally for a positive and negative magnetic field of the same amplitude. We therefore assume that the photodetector signal can be described as

$$V(t) = V_0 + V_{AC}\left|\sin(\omega t - \theta)\right| = V_0 + c\chi_0\left|\sin(\omega t - \theta)\right|, \tag{5}$$

where V_0 represents the un-modulated part of the transmitted light (used here for normalization), $V_{AC} = c\chi_0$ is the amplitude of the frequency dependent signal and c is a constant. The photodetector signal can further be expressed using the Fourier series for $|\sin(\omega t - \theta)|$, yielding

$$V(t) = V_0 + c\chi_0\left[\frac{2}{\pi} - \frac{4}{\pi}\left(\frac{1}{3}\cos(2\omega t - 2\theta) + \frac{1}{15}\cos(4\omega t - 4\theta) + \ldots\right)\right]. \quad (6)$$

Specifically, the second harmonic signal is given by

$$\begin{aligned} V_2(t) &= -\frac{4c\chi_0}{3\pi}\cos(2\omega t - 2\theta) \\ &= -\frac{4c\chi_0}{3\pi}\left(\cos(2\omega t)\cos(2\theta) + \sin(2\omega t)\sin(2\theta)\right) \\ &= -\frac{4c\chi_0}{3\pi}\left(\cos(2\omega t)\left(\cos^2(\theta) - \sin^2(\theta)\right) + 2\sin(2\omega t)\sin(\theta)\cos(\theta)\right) \\ &= -\frac{4c\chi_0}{3\pi}\left(\cos(2\omega t)\left((\tilde{\chi}')^2 - (\tilde{\chi}'')^2\right) + 2\sin(2\omega t)\tilde{\chi}''\tilde{\chi}'\right) \end{aligned} \quad (7)$$

,

where $\tilde{\chi}' = \chi'/\chi_0$ and $\tilde{\chi}'' = \chi''/\chi_0$. The lock-in detected in-phase and out-of-phase components of the second harmonic signal therefore become (rms values)

$$\begin{aligned} V_2' &= -2V_2(0)\tilde{\chi}''\tilde{\chi}' \\ V_2'' &= -V_2(0)\left((\tilde{\chi}')^2 - (\tilde{\chi}'')^2\right) \end{aligned} \quad (8)$$

where $V_2(0) = 4c\chi_0/3\sqrt{2}\pi$ is the zero frequency limit of V_2 (and V_2'').

The sign of V_{AC} depends on the optical scattering properties and the measurement geometry. For a geometry where the transmission is measured perpendicular to the axis of the applied magnetic field, as used in the present study, it is generally found that V_{AC} is negative for MNPs with sizes smaller than about 130 nm for blue laser light (λ = 405 nm). For even larger scattering entities, V_{AC} first becomes positive (*e.g.*, for 250 nm MNPs) and then negative

(*e.g.*, for 500 nm MNPs). This originates from the oscillation of the scattering cross-section with particle size as can be accounted for by Mie scattering theory.

In **Figure S2a**, the normalized in-phase and out-of-phase components of the magnetic susceptibility, extracted from the Cole-Cole model, are plotted versus frequency. In **Figure S2b**, normalized $\tilde{\chi}'\tilde{\chi}''$ and $(\tilde{\chi}')^2-(\tilde{\chi}'')^2$, have been plotted versus frequency to illustrate the shape of the two photodetector signals. The input susceptibilities, $\tilde{\chi}'$ and $\tilde{\chi}''$, are those displayed in **Figure S2a**.

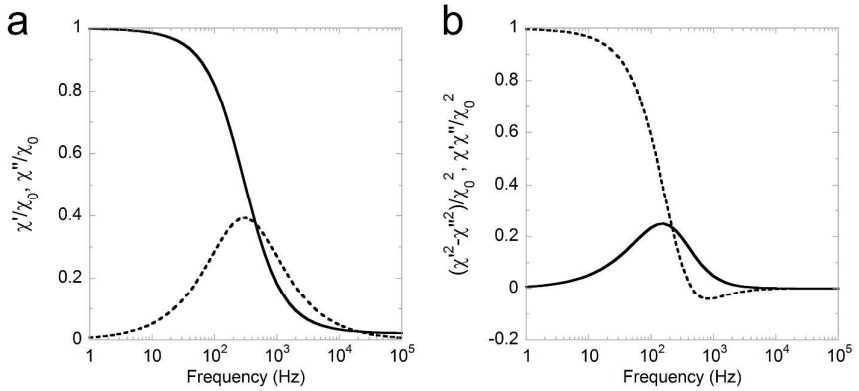

Figure S2. (a) Normalized susceptibility data (in-phase and out-of-phase represented by solid and dashed lines, respectively) extracted from the Cole-Cole model vs frequency (τ_B=300 s and α=0.15 were used as input). (b) Normalized $\tilde{\chi}'\tilde{\chi}''$ (solid line) and $(\tilde{\chi}')^2-(\tilde{\chi}'')^2$ (dashed line) vs frequency. The $\tilde{\chi}'\tilde{\chi}''$ curve represents the in-phase signal from the photodetector, whereas the $(\tilde{\chi}')^2-(\tilde{\chi}'')^2$ curve represents the out-of-phase signal from the photodetector.

Table S1. Oligonucleotide sequences of miRNAs and ssDNA probes for miRNA detection. In let-7a, c, d and e, the bases that differ from those in let-7b are marked in red.

Name	Sequence (5'→3')
let-7a	UGAGGUAGUAGGUUGUAUAGUU
let-7b	UGAGGUAGUAGGUUGUGUGGUU
let-7c	UGAGGUAGUAGGUUGUAUGGUU
let-7d	AGAGGUAGUAGGUUGCAUAGUU
let-7e	UGAGGUAGGAGGUUGUAUAGUU
Probe for let-7b	biotin-TTTTTTTTTTAACCACACAACCTACTACCTCATTTTTTTTTT-TEG-biotin
miR-21	UAGCUUAUCAGACUGAUGUUGA
Probe for miR-21	biotin-TTTTTTTTTTTCAACATCAGTCTGATAAGCTATTTTTTTTTT-TEG-biotin

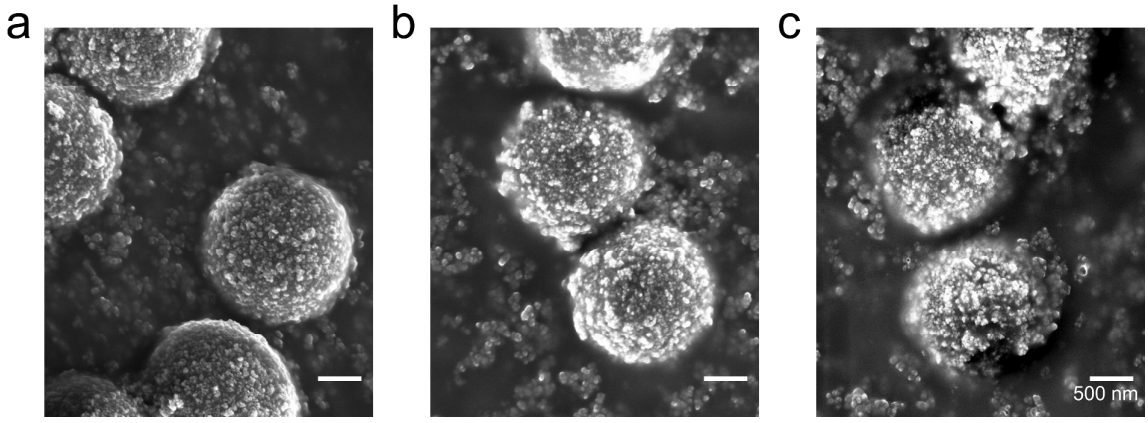

Figure S3. Scanning electron micrographs of (a) MP-NP_{80} two-layer core-satellite superstructures, (b) MP-NP_{250} two-layer core-satellite superstructures and (c) MP-NP_{250}-NP_{80} three-layer core-satellite superstructures.

S2. Determination of the binding ratios between MPs and MNPs.

Dilution series of NP_{80} with concentrations ranging from 1.56 to 50 µg/mL and of NP_{250} with concentrations ranging from 6.25 to 50 µg/mL were prepared by stepwise dilution of the stock solution with reaction buffer. The V_2'/V_0 peak amplitude (measured at 234 Hz) vs NP_{80} concentration and V_2'/V_0 valley amplitude (measured at 14 Hz) vs NP_{250} concentration are shown in **Figure S4a** and **Figure S4b**, respectively. A linear correlation between the V_2'/V_0 peak and valley amplitude vs NP concentration can be observed. The concentration of MNPs bound to the cores of the superstructures, which was utilized for calculating the binding ratio between MPs and MNPs, was determined as the final MNP concentration (concentration of MNPs after a complete reaction, **Table S2**) minus the initial MNP concentration (concentration of background MNPs before reaction, **Table S2**).

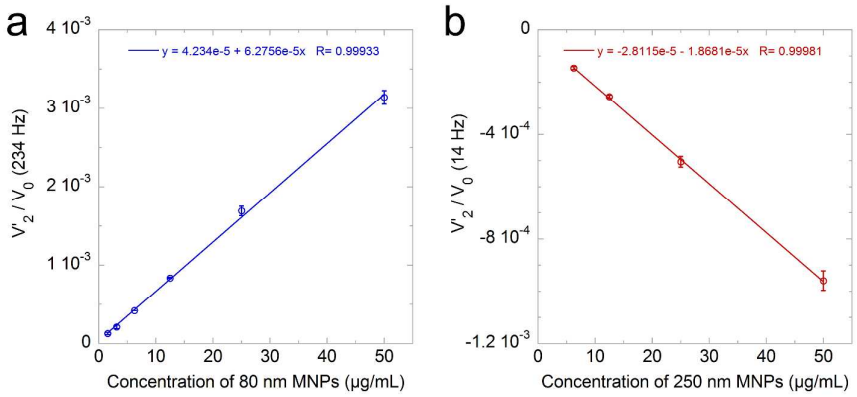

Figure S4. Standard curves for (a) NP_{80} and (b) NP_{250} suspended in reaction buffer. Error bars indicate the standard deviation of three independent replicates.

Table S2. The measured concentrations of MNPs in the initial suspension (background MNPs) and final suspension (fully released MNPs).

Superstructure	Measured MNP	Initial MNP concentration (μg/mL)	Final MNP concentration (μg/mL)
MP-NP_{80}	NP_{80}	5.39±0.27	15.64±0.52
MP-NP_{250}	NP_{250}	27.96±1.28	57.24±1.44
MP-NP_{250}-NP_{80}	NP_{80}	6.62±0.30	14.92±0.35
MP-NP_{250}-NP_{80}	NP_{250}	28.42±1.09	53.74±1.13

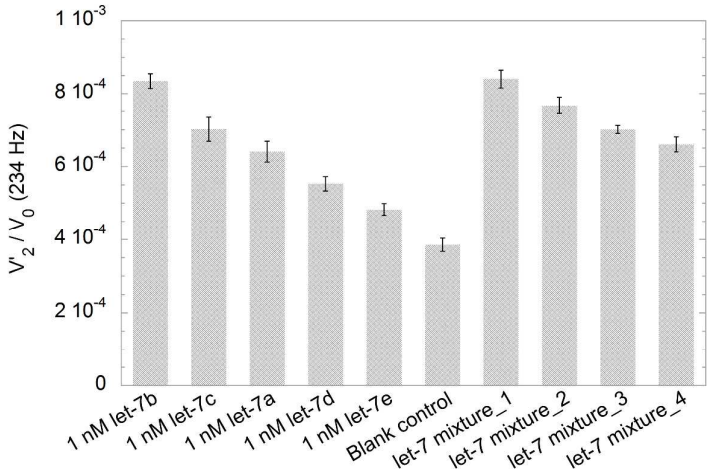

Figure S5. Specificity study of the MP-NP_{80}-based let-7b detection system. Five types of miRNAs (1 nM) in the let-7 family were measured. The let-7 mixture contained 0.25 nM each of let-7a, let-7c, let-7d and let-7e. The concentrations of let-7b were 1 nM, 0.1 nM and 10 pM in let-7 mixture_1, let-7 mixture_2 and let-7 mixture_3, respectively. The let-7 mixture_4 did not contain let-7b. Error bars indicate the standard deviation of three independent replicates.

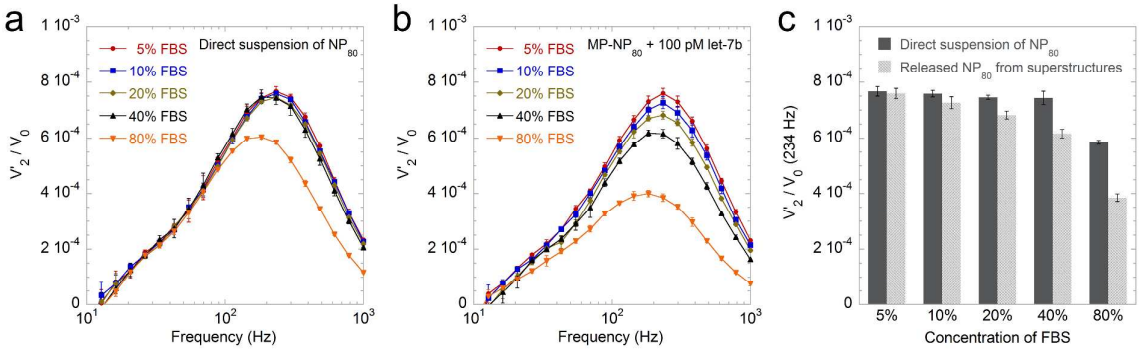

Figure S6. Stability study of the optomagnetic detection system in fetal bovine serum (FBS). (a) Optomagnetic spectra of direct NP_{80} measurement in 5%, 10%, 20%, 40% and 80% FBS. (b) Optomagnetic spectra of MP-NP_{80}-based detection system for the measurement of 100 pM let-7b in 5%, 10%, 20%, 40% and 80% FBS. (c) Bar graph of the optomagnetic signal at 234 Hz for direct NP_{80} measurement and MP-NP_{80}-based let-7b detection in diluted FBS samples. Error bars indicate the standard deviation of three independent replicates.

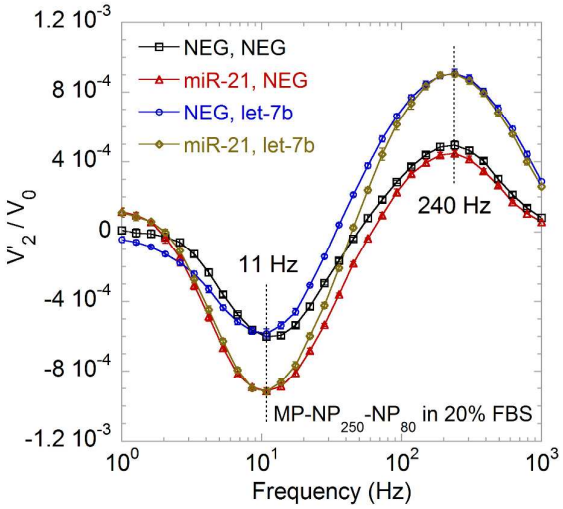

Figure S7. Qualitative duplex detection in 20% fetal bovine serum. Two target miRNAs, miR-21 and let-7b, were detected simultaneously using MP-NP_{250}-NP_{80} superstructures. The spectra are characterized by valleys/peaks located at 11 Hz and 240 Hz, respectively, corresponding to the released nanoparticles. NEG: absence of target miRNA (only reaction buffer). Error bars indicate the standard deviation of three independent replicates.

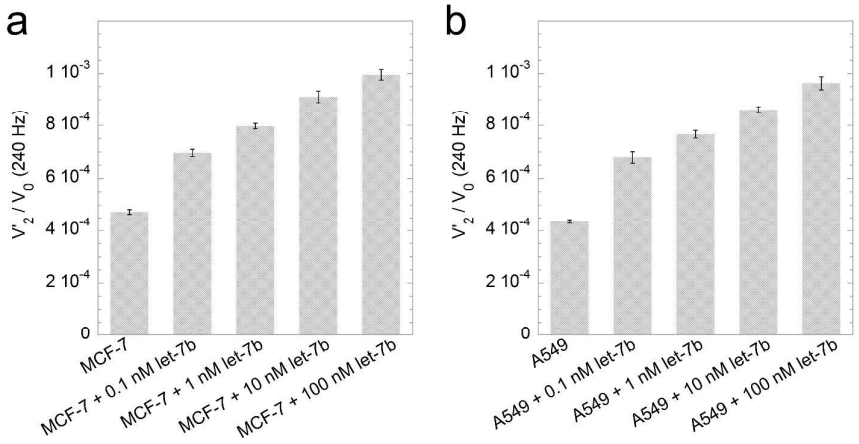

Figure S8. Detection of endogenous let-7b from human cancer cells MCF-7 (a) and A549 (b). V_2'/V_0 peak amplitude (measured at 240 Hz) was obtained from diluted total RNA extracts spiked with different concentrations of let-7b. The concentrations of spiked let-7b were 0.1, 1, 10 and 100 nM. Error bars indicate the standard deviation of three independent replicates.

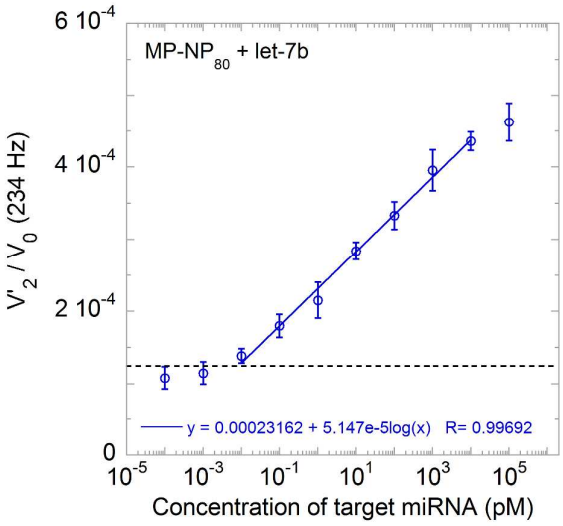

Figure S9. Quantitative singleplex detection of let-7b using filter-treated MP-NP_{80} superstructures. Error bars indicate the standard deviation of three independent replicates.

REFERENCE

(1) Cole, K. S.; Cole, R. H. Dispersion and Absorption in Dielectrics I. Alternating Current Characteristics. *J. Chem. Phys.* **1941,** *9*, 341-351.